The role of deviatoric stress and dislocations on the to phase transformation in Ti

Dang, Khanh Quoc
Tome, Carlos
Capolungo, Laurent

To be published in: Acta Materialia

DOI to publisher's version: 10.1016/j.actamat.2022.118510

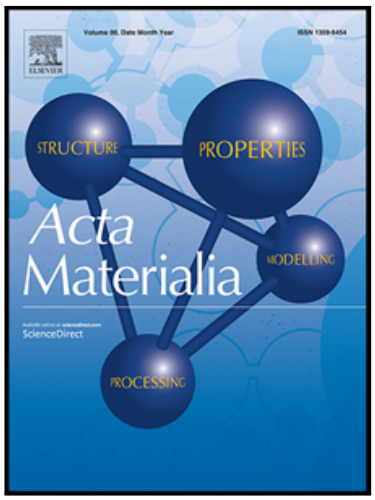

The role of deviatoric stress and dislocations on the α to ω phase transformation in Ti

Khanh Dang , Carlos N. Tomé , Laurent Capolungo

PII: S1359-6454(22)00887-4
DOI: https://doi.org/10.1016/j.actamat.2022.118510
Reference: AM 118510

To appear in: *Acta Materialia*

Received date: 10 June 2022
Revised date: 31 October 2022
Accepted date: 9 November 2022

Please cite this article as: Khanh Dang , Carlos N. Tomé , Laurent Capolungo , The role of deviatoric stress and dislocations on the α to ω phase transformation in Ti, *Acta Materialia* (2022), doi: https://doi.org/10.1016/j.actamat.2022.118510

The role of deviatoric stress and dislocations on the α to ω phase transformation in Ti

Khanh Dang,[a] Carlos N. Tomé,[a] and Laurent Capolungo[a]

[a] MST-8, Los Alamos National Laboratory, Los Alamos, NM 87544, USA

Graphical abstract

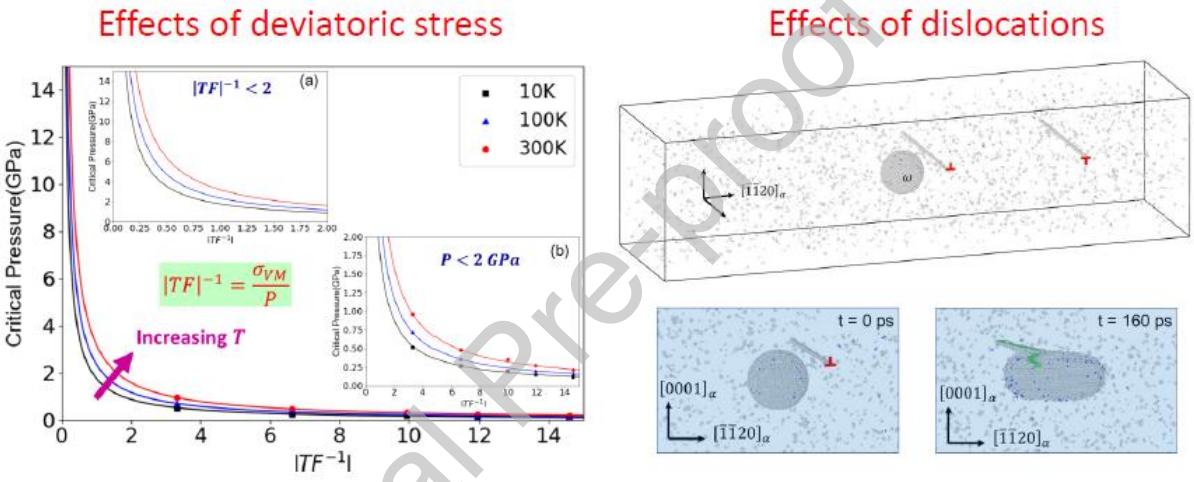

Abstract

Under extreme conditions, α-Ti becomes unstable and transforms either into β-Ti at high temperature or into ω-Ti at high pressure. In what concerns the α to ω phase transformation (PT), there has been a wide range of experimentally reported transition pressures from approximately 2 to 15 GPa at room temperature. Deviatoric stresses and internal defects are often assumed to be the root cause of this variation. In this study, these postulates are revisited using both continuum mechanics and molecular dynamics (MD) simulations. First, a simple continuum model, assuming linear elasticity and isotropic plasticity, is developed to describe the effects of applied stress and dislocations on the stability of an ω nucleus in an infinite α domain. Second, a new MD simulation method is developed to generate an ω nucleus in the α domain utilizing the displacement field identified from the topological analysis. Results from MD simulations show that

despite the fact that phase diagrams typically delineate the limits between two phases in terms of only P and T, deviatoric stress promotes the α to ω phase transformation by reducing the critical radius above which an ω nucleus is stable. Furthermore, the required deviatoric stress to nucleate and stabilize a nanoscale ω nucleus is likely emanating from the internal stress of defects such as dislocations. The MD-informed micromechanics models are used to identify favorable configurations where dislocations help favor the α to ω transformation. These configurations show that the interaction with a basal or prismatic dislocation reduces the critical radius of a ω nucleus by about 10 or 16 %, respectively. In addition, prismatic edge dislocations are found to promote the growth of ω nucleus when interacting with the $(\bar{1}\bar{1}20)_\alpha//(0001)_\omega$ interface. Importantly, a simple model of the arrival of dislocation at an ω nucleus suggests that PT does not necessarily require a pile-up to be present but could alternatively be mediated by a constant rapid flow of dislocations.

Keywords: Phase transformation, α -Ti, HCP, ω-Ti, Molecular Dynamics Simulations

1. Introduction

Due to its lightweight and high strength, Ti and its alloys are finding a wide range of structural applications. The plastic response of Ti is complex and mediated by multiple deformation modes. Specifically, at room temperature, due to the limited number of easily activated slip systems, twinning is often the only deformation mode available that will accommodate strain parallel to the c-axis [1–3]. Further, under extreme conditions, α-Ti (hexagonal close packed (HCP)) becomes unstable and transforms into β-Ti (body centered cubic (BCC)) (at high temperature) or ω-Ti (ω hexagonal) (at high pressure) as seen typically illustrated in phase diagrams [4]. For automotive and aerospace applications, the pressure-induced martensitic phase transformation (PT) from α to ω is important since ω-Ti is harder and more brittle than α-Ti and can thus deteriorate the mechanical performance of the parts during operation [5–7]. Therefore, there has been a great number of works aimed at understanding this martensitic/ first order PT, focusing on the equation of state, the crystallography of the PT, the transformation orientation relationship (OR) and potential pathways from α to ω.

Experimentally, the α to ω PT was observed in static high pressure or dynamic shock loading in Ti and Zr, where the transformation pathways are inferred by the orientation relationships (ORs) between the parent and product phases [8–11]. These transformation pathways can also be identified using density functional theory (DFT) calculations [4,12]. Overall, two main ORs have been reported for α to ω PT in Ti and Zr. In seminal work, Silcock proposed that there is a direct transformation pathway from α to ω, where the final OR follows $\{0001\}_\alpha // \{1\bar{2}10\}_\omega$ and $[1\bar{2}10]_\alpha // [0001]_\omega$ [8]. This OR was also observed by Rabinkim et al. via Transmission Electron Microscopy (TEM) study of

Zr α to ω induced by high pressure [9] and more recently in pressure and high-pressure torsion (HPT) studies of Zr [10,11]. The 2nd OR, $\{0001\}_\alpha//\{01\bar{1}1\}_\omega$ and $[11\bar{2}0]_\alpha//[10\bar{1}1]_\omega$, where α transform to ω indirectly via the intermediate β phase, was first suggested by Usikov and Zilbershtein [13]. This was later identified as the lowest energy pathway via ab-initio calculations for Ti [4]. A direct deformation pathway involving a similar OR with $\{0001\}_\alpha//\{10\bar{1}1\}_\omega$ and $[10\bar{1}0]_\alpha//[11\bar{2}\bar{3}]_\omega$ was reported by Song and Gray [14]. While these two ORs are frequently observed and widely accepted, there has been an ongoing debate about the differences between reported transition pressure.

Specifically, there has been a wide range of experimentally reported α to ω transition pressures from approximately 2 to 15 GPa at room temperature depending on the loading conditions and sample purity [7,15–20]. This variation is often explained by (1) non-hydrostatic stress states superimposed on pressure, and (2) pre-existing impurities or defects. Zhang et al. proposed a novel formalism to incorporate the non-hydrostatic stress state into the constitutive relations and used it to quantify the effects of shear stresses on the transition pressure of the martensitic α to ω PT in Ti [20]. However, the formalism does not account for the effect of impurities or defects which, in practice, can influence the equation of state and thus the transition pressure for PT. For instance, increasing the O content of Ti alloy can increase the transition pressure from 10.4 GPa to at least 35 GPa with no transformation observed [18]. In another work, Levitas proposed that high-pressure PT should be categorized into either pressure-induced, stress-induced, or strain-induced PTs. Especially for strain-induced PTs, the stress from defects such as dislocation as part of a pile-up against grain boundaries can help reduce significantly the transition pressure because the local stress at interfaces can be much

greater than the average equilibrium stress [21,22]. In parallel to those theoretical developments, there have been several 2D modelling studies using nanoscale [23–25] and scale-free phase field simulations [26,27] focusing on the interactions between dislocations and their effects on the nucleation of high-pressure PTs. Specifically, these studies focused on understanding phase nucleation (e.g. morphology of multiple nucleii), phase evolution and coalescence as well as arrest in the absence and in the presence of dislocations. However, so far there has not been any comprehensive 3D study of dislocation effects on high-pressure PTs.

Thus, here we study the effects of non-hydrostatic stress and dislocations on the α to ω PT in Ti using both continuum mechanics and molecular dynamics (MD) simulations. We hypothesise that the α to ω martensitic PT is strain-induced, according to the nomenclature proposed by Levitas [21], and its nucleation can depend on the arrival rate of dislocations. First, we developed a simple continuum model with linear elasticity and isotropic plasticity to describe the effects of applied stress and defects on the stability of the ω nucleus in the α domain. The main difference between our model and that of Levitas [21] lies in the full 3D treatment of the elastic response instead of 2D plane stress assumptions. This consideration is critical since the transformation strain for the α to ω PT contains three diagonal anisotropic components. Second, we created a new method in MD simulations to generate a ω nucleus in the α domain utilizing the displacement field identified from the topological analysis. This allows us to (1) show the effects of deviatoric stress components on the stability of the ω nucleus and (2) calibrate our micromechanics model with results from MD simulations. Finally, the effects of basal and prismatic dislocations on the stability and growth of the ω nucleus are explored.

Our results show that deviatoric stress is required for the α to ω transformation to take place and that this deviatoric stress may likely originate from dislocations. Moreover, it is found that both prismatic and basal dislocations can help to promote the ω growth by reducing its critical stability radius. An alternative dynamic process of how incoming dislocation with appropriate arrival rates can help to stabilize the ω nucleus to go from subcritical to the critical size is thus presented. Furthermore, only prismatic dislocations were found to influence the growth of the ω nucleus once it surpasses its critical size.

2. Energetic considerations for the stability of ω nucleus in α domain

To understand the role of dislocations and deviatoric stresses in the α-ω phase transformation, we consider the configurations shown in Fig. 1 where the ω nucleus is formed inside the α matrix. Here, the ω nucleus is assumed to be a sphere with radius R because upon relaxation (via MD simulations) it quickly adopts a faceted energy-minimization configuration, independently of the initial shape. A pile-up of n_{dis} dislocations is placed D1 (nm) away from the center of the ω nucleus at an angle θ. Here, we only consider the α-ω phase transformation proposed by Silcock, where $(0001)_\alpha//(2\bar{1}\bar{1}0)_\alpha$, $[\bar{1}\bar{1}20]_\alpha//[0001]_\omega$, which is commonly observed in experimental and modelling studies of Ti [4,8,28–30]. Specifically, this deformation pathway and orientation have been observed in Ti under nonequilibrium molecular dynamics (NEMD) shock simulations [30] using a Ti MEAM potential [31]. Moreover, the construction of the ω nucleus for the Silcock deformation pathway does not involve the out-of-plane shuffle, which makes it simpler than the other deformation pathway.

Ultimately, our goal is to determine the configurations which are more favorable to the formation and growth of ω nucleus. In order to achieve this, it is necessary to map out the Gibbs free energy landscape of the configurations with respect to the applied stress (σ_o) (which can be decomposed into hydrostatic (P) and deviatoric components (σ_{dev})), the number of dislocations (n_{dis}), and the location of the dislocations (D_1 and θ) with respect to the inhomogeneous inclusion. This allows calculating the difference in free energy between a configuration with an ω nucleus of a specific size and under applied stress (σ_o) and the one without. This is the change in the Gibbs free energy between the two systems, which determines whether it is more energetically favorable for the ω nucleus to form and grow. Understanding how the different parameters describing the system's configuration affect this change in Gibbs free energy will allow one to determine the role of dislocations and loading conditions on the α-ω PT. Those configurations are then constructed and validated by MD simulations in Section 3.

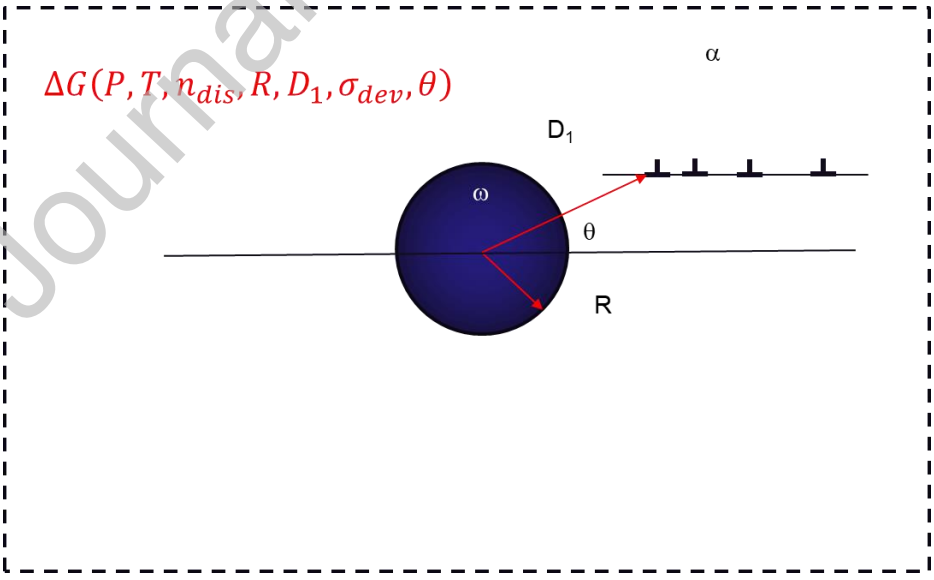

Figure 1. Configurations of the ω nucleus inside the α matrix for type 2 transformation with the incoming dislocation pile-up.

2.1 ω nucleus as an Eshelby inhomogeneous inclusion inside the α domain

To analyze the thermodynamic landscape associated with an ω nucleus as an inhomogeneous inclusion inside the α matrix, we adopt the standard Eshelby approach where the ω nucleus is treated as an inhomogeneous inclusion with elastic constants (C^*_{ijkl}) embedded in an α matrix with constants (C_{ijkl}). In addition, there is a transformation eigenstrain ε^{tr}_{kl} [32,33]. This approach has been used to study the role of the stress state in the nucleation and propagation of twinning in several systems [33]. Note that the model relies on simplifying assumptions such as linear elasticity and small strains. As a consequence, it is used in a qualitative manner, meant to identify the relative weight of the different factors and the main trends of the system and to guide the MD quantitative characterization. Here, the reference frame is such that the X, Y, and Z directions align with the $[\bar{1}\bar{1}20]_\alpha$, $[1\bar{1}00]_\alpha$, and $[0001]_\alpha$ directions. For the Silcock PT the ω nucleus is oriented such that the X, Y, and Z directions align with the $[0001]_\omega$, $[0\bar{1}10]_\omega$, and $[2\bar{1}\bar{1}0]_\omega$ directions. In what follows, we will review the general Eshelby treatment for the inhomogeneous inclusion problem. More details can be found in [32]. Einstein summation convention over repeated indices is utilized for all expressions in the following discussion.

For a system under a uniform strain ε^o due to the uniformly applied stress σ^o, the stress inside the inhomogeneous inclusion can be equivalently written as:

$$\sigma^o_{ij} + \Delta\sigma_{ij} = C^*_{ijkl}(\varepsilon^o_{kl} + \Delta\varepsilon_{kl} - \varepsilon^{tr}_{kl}) \qquad \text{(Equation 1)}$$

where $\Delta\sigma$ and $\Delta\varepsilon$ are the perturbations to the stress and strain caused by the inhomogeneous inclusion. The transformation strain (ε^{tr}) is the strain that takes place when transforming from α to ω. One approach to solve the inhomogeneous inclusion problem is to use the equivalent homogeneous inclusion with an additional fictitious transformation strain (ε^{*}) which is determined via the use of the Eshelby solution. The stress inside the inhomogeneous inclusion then can be rewritten as:

$$\sigma_{ij}^{o} + \Delta\sigma_{ij} = C_{ijkl}(\varepsilon_{kl}^{o} + \Delta\varepsilon_{kl} - \varepsilon_{kl}^{tr} - \varepsilon_{kl}^{*}) \quad \text{(Equation 2)}$$

Importantly, the deviation of the strain due to the inhomogeneous inclusion is related to the sum of the transformation and fictitious strains $\varepsilon_{mn}^{**} = (\varepsilon_{mn}^{tr} + \varepsilon_{mn}^{*})$ such as:

$$\Delta\varepsilon_{kl} = S_{klmn}\varepsilon_{mn}^{**} \quad \text{(Equation 3)}$$

where S_{klmn} is the Eshelby tensor. Here, the inhomogeneous inclusion is assumed to be a sphere and the standard Eshelby solution dictates that the stress field is homogeneous for an ellipsoidal-shaped inclusion [32]. Defining the difference in elastic stiffness tensor as $\Delta C_{ijkl} = C_{ijkl}^{*} - C_{ijkl}$ and substituting it into Eqs. (1) and (2), one can derive the following expression:

$$\left(\Delta C_{ijkl}S_{klmn} + C_{ijmn}\right)\varepsilon_{mn}^{**} = -\Delta C_{ijkl}C_{klmn}^{-1}\sigma_{mn}^{o} + C_{ijkl}^{*}\varepsilon_{kl}^{tr} \quad \text{(Equation 4)}$$

where S_{klmn} is the Eshelby tensor. This expression allows one to calculate the fictitious strain (ε^{*}) and eventually, the perturbations to the stress and strain ($\Delta\sigma$ and $\Delta\varepsilon$) caused by the inhomogeneous inclusion as a function of the applied stress tensor.

These elastic responses are then used to calculate the variation in Gibbs free energy between the system with and without the inhomogeneous inclusion. This gives an

estimate of the energy barrier for the formation of the inhomogeneous inclusion. The change in Gibbs free energy due to the inhomogeneous inclusion is given by

$$\Delta G = G_1 - G_o = E_1 + \Gamma - E_o + \Delta E_{ch} \qquad \text{(Equation 5)}$$

where E_o and E_1 are the elastic strain energy of the systems without and with the inhomogeneous inclusion, while Γ is the total interfacial energy of the interfaces shared between the inhomogeneous inclusion and the matrix. ΔE_{ch} is the total change in chemical free energy between the inhomogeneous inclusion and the matrix. ΔE_{ch} is often calculated as $V\Phi_{ch}$, where $\Phi_{ch}$is the change in chemical free energy per unit volume of the transformation. Due to the lack experimental data quantifying Φ_{ch} , MD results from a study published in the literature are used to estimate this chemical energy change. The MD study used the rapid artificial neural network (RANN) potential. It was shown that this potential can replicate pressure-temperature phase diagram (see Fig. 6b of [34]). The results of this study, duplicated in the Figure R1 below, show that the change in chemical free energy per unit atom for the α–ω PT in Ti at 300K is approximately 7.9 meV/atom, which translates to Φ_{ch} ≈0.45 meV/Å^3.The Gibbs free energy of a medium undergoing a transformation strain (ε_{kl}^{tr}) under an externally applied stress (σ_{ij}^{o}) is given by

$$E_1 + \Gamma = \frac{1}{2}\int_D \left(\sigma_{ij}^o + \Delta\sigma_{ij}\right)(\varepsilon_{kl}^o + \Delta\varepsilon_{kl} - \varepsilon_{kl}^{tr})\, dD - \int_S F_i(u_i^o + \Delta u_i)\, dS + 4\pi R^2\gamma \qquad \text{(Equation 6)}$$

where F_i are the components of the external surface traction, u_i^o is the displacement if F_i acts alone, and Δu_i is the displacement induced by the inhomogeneous inclusion. D and S are the volume and external surface of the medium, respectively. From the derivation by Mura [24], the elastic strain energy of the systems with the inhomogeneous inclusion transforms into

$$E_1 = \frac{1}{2}\int_D \sigma_{ij}^o \varepsilon_{ij}^o \, dD - \frac{1}{2}\int_\Omega \Delta\sigma_{ij}\varepsilon_{ij}^{tr} \, dD + \frac{1}{2}\int_\Omega \sigma_{ij}^o \varepsilon_{ij}^* \, dD - \int_S F_i(u_i^o + \Delta u_i) \, dS \quad \text{(Equation 7)}$$

where Ω is the volume of the inhomogeneous inclusion. Moreover, the Gibbs free energy for the inclusion-free homogenous medium is given by

$$E_o = \frac{1}{2}\int_D \sigma_{ij}^o \varepsilon_{kl}^o \, dD - \int_S F_i u_i^o \, dS \quad \text{(Equation 8)}$$

From Eqs (6), (7), and (8), one can calculate the change in Gibbs free energy due to the inhomogeneous inclusion as:

$$\Delta G = \left(-\frac{1}{2}\int_\Omega \Delta\sigma_{ij}\varepsilon_{ij}^{tr} \, dD - \frac{1}{2}\int_\Omega \sigma_{ij}^o \varepsilon_{ij}^* \, dD - \int_\Omega \sigma_{ij}^o \varepsilon_{ij}^{tr} \, dD\right) + 4\pi R^2\gamma + \Delta E_{ch} \text{(Equation 9)}$$

Here, γ is the average surface energy. Importantly, this expression allows calculating the minimum energy barrier required to stabilize an inhomogeneous inclusion as a function of size and externally applied stresses.

2.2 Effects of dislocations on the stability of the inhomogeneous inclusion

To understand the effects of dislocations on the stability of the inhomogeneous inclusion, the variation in Gibbs free energy ($\Delta G_{2\to3}$) between a system which contains dislocations but no inhomogeneous inclusion (G_2), and another with an inhomogeneous inclusion (G_3) is determined. In addition to these two systems, Fig. 2 shows another two systems with no dislocation: one with no inhomogeneous inclusion (G_o), and another with an inhomogeneous inclusion (G_1). Based on Fig. 2, the variation in Gibbs free energy between the systems with dislocations ($\Delta G_{2\to3}$) can be related to one without dislocations ($\Delta G_{0\to1}$).

$$\Delta G_{2\to3} = W_1 + \Gamma - W_o + E_{int} = \Delta G_{0\to1} + E_{int} \quad \text{(Equation 10)}$$

, where E_{int} is the total interaction energy between the dislocations and the inhomogeneous inclusion. This can be determined by integrating the individual interaction energy at every point within the inhomogeneous inclusion. For this study, the interaction energy density is assumed to be homogenous within the inhomogeneous inclusion and equal to the interaction energy between the dislocation and the center of the inhomogeneous inclusion. This simplification necessarily degrades the accuracy of the prediction but allows one to find an analytical solution to this problem. This interaction energy is treated akin to that between a dislocation and the point defect [35]. Here, only the first-order size interaction (based on linear elasticity assumption) is considered since it is dominant compared to the second-order size interaction and the inhomogeneity interaction. The second-order size interaction appears when considering the third-order (non-linear) elastic properties of the crystal. The inhomogeneity interaction occurs when the elastic inclusion which has elastic constants that significantly differ from the corresponding elastic constants of the matrix. For this study, the second-order size and the inhomogeneity interactions are negligible compared to the first-order size interaction. Only edge dislocations are considered since the core energy of the edge dislocation is larger than the screw dislocation, and is thus believed to have higher interaction energy with the inhomogeneity. The first-order interaction between a pile-up of straight edge dislocations and a spherical inhomogeneous inclusion is given by Bullough and Newman [25]:

$$E_{int} = 4\mu b\varepsilon R^3 \sum_{k=1}^{ndis} \frac{sin\phi_k}{D_k} = 4\mu b\varepsilon R^3 \sum_{k=1}^{ndis} \frac{sin(\theta_k+\pi)}{D_k} \qquad \text{(Equation 11)}$$

where μ is the elastic shear modulus of the medium, b is the Burgers vector, ϕ_i and R_{1i} define the relative position of the point defect (inhomogeneous inclusion) with respect to

the dislocation, respectively, n_{dis} is the number of dislocations in the pile-up, and ε is the radial component of the transformation strain tensor in the spherical coordinate. Combining Eqs. (9), (10), and (11), the general expression for the change in Gibbs free energy for the configuration shown in Fig. 1 is given by

$$\Delta G = -\frac{4}{3}\pi R^3\left(\frac{1}{2}\Delta\sigma_{ij}\varepsilon_{ij}^{tr} + \frac{1}{2}\sigma_{ij}^{o}\varepsilon_{ij}^{*} + \sigma_{ij}^{o}\varepsilon_{ij}^{tr}\right) + 4\pi R^2\gamma + 4\mu b\varepsilon R^3\sum_{k=1}^{ndis}\frac{sin(\theta_k+\pi)}{D_k} + \frac{4}{3}\pi R^3\Phi_{ch}$$

(Equation 12)

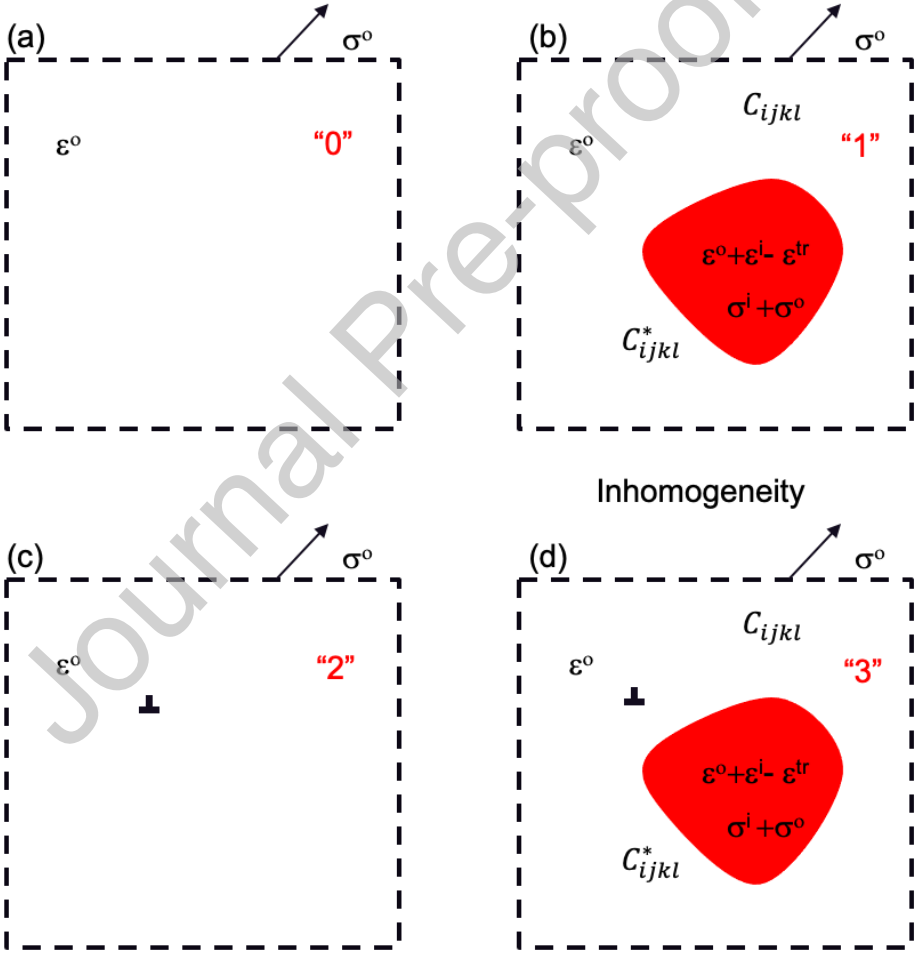

Figure 2. Systems with (a) neither dislocation nor inhomogeneous inclusion, (b) with an inhomogeneous inclusion but no dislocation, (c) with a dislocation but no

inhomogeneous inclusion, and (d) with both dislocation and inhomogeneous inclusion under an applied external stress tensor σ_o .

2.3 The critical radius of the ω nucleus

The critical stability radius of the ω nucleus (R_c) is defined by the condition of maximum in the change in Gibbs free energy and can be determined by solving the following system [23]:

$$\left.\frac{\partial(\Delta G)}{\partial R}\right|_{R_c} = 0 \quad \text{and} \quad \left.\frac{\partial^2(\Delta G)}{\partial R^2}\right|_{R_c} < 0 \qquad \text{(Equation 13)}$$

Substituting Eq. (12) into the equality part of Eq. (13), the critical radius of the ω nucleus can be expressed as:

$$R_c = \frac{4\gamma}{\Delta\sigma_{ij}\varepsilon_{ij}^{tr} + \sigma_{ij}^{o}\varepsilon_{ij}^{*} + 2\,\sigma_{ij}^{o}\varepsilon_{ij}^{tr} - \frac{6\mu b\varepsilon}{\pi}\sum_{k=1}^{ndis}\frac{\sin(\theta_k+\pi)}{D_k} - 2\Phi_{ch}} \qquad \text{(Equation 14)}$$

Substituting this R_c into the inequality part of Eq. (13), one obtains $\left.\frac{\partial^2(\Delta G)}{\partial R^2}\right|_{R_c} = -2\gamma < 0 \; for \; \gamma > 0$, which is always satisfied since the average surface energy is always positive. In addition to R_1 and θ_1, the relative location of each dislocation in the pile-up with respect to the center of the nucleus is also a function of the equilibrium distance between the dislocations under an applied shear stress [36]. Note that while Eq.14 offers insights on the thermodynamics of growth and stabilization, it does not provide details about the nucleation process (activation volume, energy barrier, and pathway). Thermally activated nucleation is also not considered in this work. Eq.14 allows one to determine the critical radius of the ω nucleus for different configurations of applied stress and relative location of the dislocation with respect to the center of the nucleus. Depending on the

relative position between the dislocation and the nucleus (θ_i), the interaction can be attractive or repulsive. For $0 < \theta_i < \pi$, the interaction is attractive and thus reducing the critical radius beyond which the ω nucleus will grow. On the other hand, for $\pi \leq \theta_i \leq 2\pi$, the interaction is repulsive, which increases the critical radius, thus, hindering the growth of the ω nucleus. In Eq. (14), the average/effect interface energy is unknown. It will be determined by fitting to MD results in Section 3

2.4 Hypotheses on how dislocations can influence the stability and mobility of the ω nucleus

As shown in Fig. 3, depending on whether the nucleus is below or above the critical size, there are two circumstances for which the dislocation can influence the stability and mobility of the ω nucleus. Eq. (14) shows that the interaction energy between the dislocation and the nucleus can reduce the critical size of the nucleus. In this subcritical regime, there are two possible scenarios: (1) the dislocations pile up and the stress field ahead of this pile-up would reduce the critical size of the nucleus, as shown in previous works [21,22], or (2) the dislocations travel near the nucleus and their interactions help to grow the nucleus from subcritical to a critical size, at which point the growth is energetically preferred. The former scenario is more “static”, requires a large number of dislocations, and has been demonstrated by previous studies using a combined approach of micromechanics and MD simulations [21,22]. Here, we focus on the latter scenario with a more dynamic requirement of the dislocation motion but potentially requiring fewer dislocations to be involved in the process. Furthermore, the role of dislocations in the mobility of the ω nucleus once its size surpasses the critical value is also investigated as shown schematically in Fig. 3b.

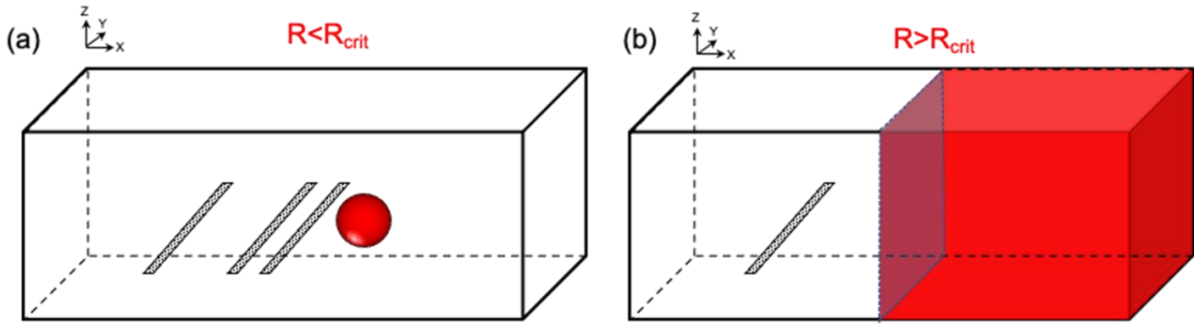

Figure 3. Different scenarios for dislocation ω nucleus interaction where (a) the nucleus is in the subcritical regime and will collapse without the interaction with dislocations and (b) the nucleus size exceeds the critical value and will grow regardless of the interaction with the dislocations.

3. MD simulations

3.1 Topological analysis

A topological analysis via the coherent dichromatic complex (CDC) of the strained α and unstrained ω lattices, is shown in Fig. 4. The same reference system of the α matrix is used such that the X, Y, and Z directions align with the $[\bar{1}\bar{1}20]_\alpha$, $[1\bar{1}00]_\alpha$, and $[0001]_\alpha$ directions. The α lattice is strained via a transformation strain of $\varepsilon_{tr} = \begin{pmatrix} -0.039 & 0 & 0 \\ 0 & 0.049 & 0 \\ 0 & 0 & -0.015 \end{pmatrix}$ to ensure that the lattice sites of both lattices coincide. Four different types of atoms can be categorized based on their coordinates along the $[0001]_\alpha$//$[2\bar{1}\bar{1}0]_\omega$ directions. Circles and triangles represent the top and bottom layers, respectively. Solid blue circles are HCP (α) atoms, while red hollow circles are ω hexagonal atoms. Based on results from Fig. 4, one can map out the displacement field to transform the HCP (α) lattice into ω lattice. The displacement vectors are all equal in magnitude and have components of 0.0704 nm in the $[1\bar{1}00]_\alpha$ direction and 0.022 nm in

the $[\bar{1}\bar{1}20]_\alpha$direction. The relative small strain and shuffle displacement vectors help to explain why this OR ($\{0001\}_\alpha//\{1\bar{2}10\}_\omega$) is commonly observed in Ti. This strain and displacement field is then used to generate a ω nucleus in the α matrix.

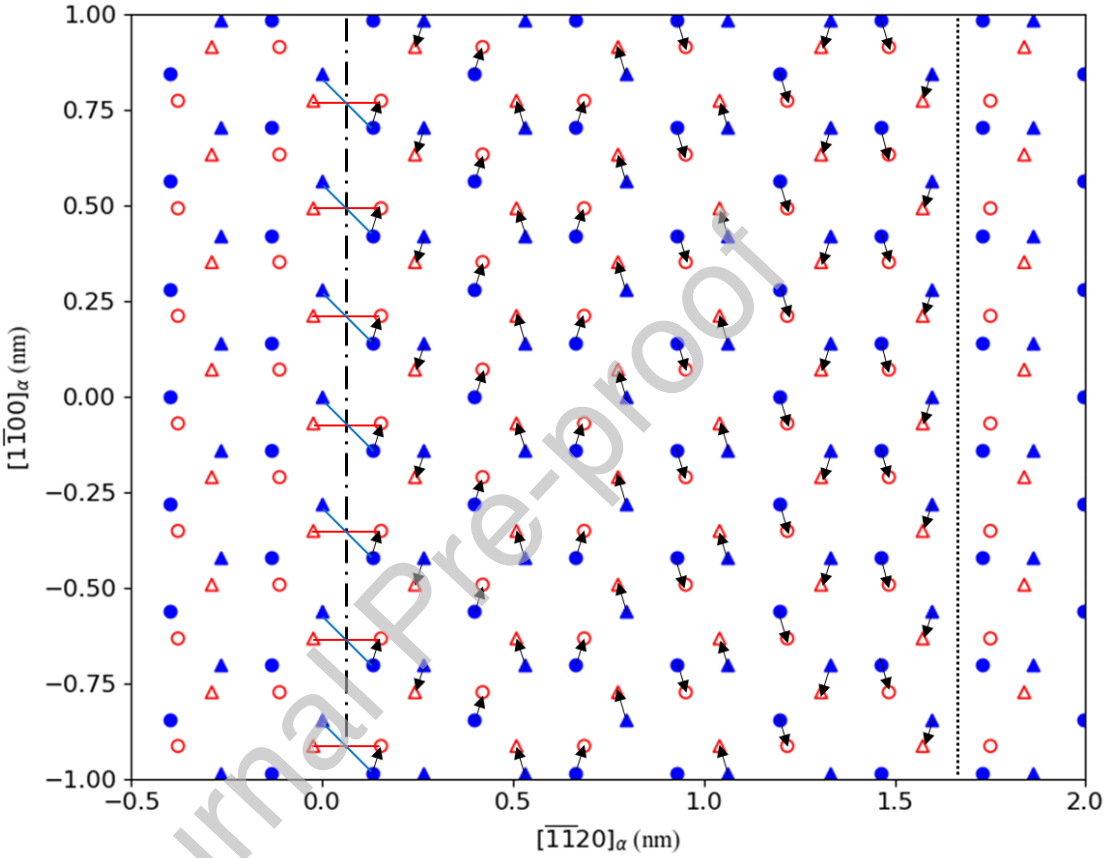

Figure 4. The coherent dichromatic complex (CDC) of the ω phase within the α domain viewed along the $[0001]_\alpha//[2\bar{1}\bar{1}0]_\omega$ direction. Blue solid atoms are α (HCP) atoms. Red hollow atoms are ω atoms. The black dash-dot line is along the $[1\bar{1}00]_\alpha$ direction.

3.2 Simulation setup

All atomistic simulations are performed using the classical atomistic simulation code LAMMPS. To model Ti systems, the modified embedded atom method (MEAM) interatomic potential developed by Hennig [31] is used since it can accurately reproduce defect properties such as surface energy and energy barriers for the homogeneous

martensitic transformations. The potential underpredicts the I_2 stacking fault energy, and thus would overpredict the dissociated distance of the <a> dislocation on the basal plane. Another drawback of using this potential is that it is computationally expensive and thus limits the size of the simulation domains (to approximately 50-100 nm). The Open Visualization Tool (OVITO) is used to analyze and visualize the results from MD simulations [37].

Several configurations with and without dislocations are used for the MD simulations. To study the role of deviatoric stresses in the stability of the ω nucleus (without dislocation), a cube simulation cell is used. The simulation cell is oriented such that the X, Y, and Z axes are along the $[\bar{1}\bar{1}20]_\alpha$, $[1\bar{1}00]_\alpha$, and $[0001]_\alpha$ directions. Periodic boundary conditions are applied in all directions. Two different sizes of 30x30x30 nm and 50x50x50 nm (containing approximately 1.5 and 10 million atoms) are used to determine if there are image force effects on the simulation results. The ω nucleus is generated by applying the transformation strain $\varepsilon_{tr} = \begin{pmatrix} -0.039 & 0 & 0 \\ 0 & 0.049 & 0 \\ 0 & 0 & -0.015 \end{pmatrix}$ and subsequent displacement field based on the topological analysis of the simulation cell. This allows generating a nucleus with any geometry and dimension. In this work, only a spherical nucleus is considered since preliminary simulations with different nucleus geometry shows the same growth and collapse behaviors of the nucleus. First, the stability of a spherical ω nucleus with a constant radius of 5nm is investigated under different applied stress tensors at 3 different temperatures (10K, 100K, and 300K) using a Nosé-Hoover style thermostat and barostat [38] for 400 ps. The stabilizing stress tensor is determined for each temperature using the bisection method with the initial guess for the stress tensor

determined extracted from the thermo elastic-plastic self-consistent (EPSC)-type simulations. Then, for each temperature, the stabilizing stress tensor is decomposed into the hydrostatic and deviatoric components. To describe the relative degree of hydrostatic stress in a given stress state, the stress triaxiality factor is used:

$$TF = \frac{P}{\sigma_{VM}} = \frac{-\frac{1}{3}(\sigma_{11}+\sigma_{22}+\sigma_{33})}{\sqrt{\frac{(\sigma_{11}-\sigma_{22})^2+(\sigma_{22}-\sigma_{33})^2+(\sigma_{33}-\sigma_{11})^2+6(\sigma_{12}^2+\sigma_{23}^2+\sigma_{31}^2)}{2}}} \quad \text{(Equation 15)}$$

where P is the pressure and σ_{VM} is the von Mises stress, which is zero for hydrostatic pressure states. The pressure is defined such that positive pressure is compressive and negative pressure is tensile. For convenience, we define the inverse stress triaxiality factor (denoted as TF^{-1}) as the ratio between the Von Mises (deviatoric) stress and the pressure, such that $TF^{-1} = 0$ for hydrostatic pressure states. Different stress tensors with a wide range of deviatoric components, corresponding to $2 < TF^{-1} < 17$ are used.

Second, only two inverse stress triaxiality factors of 1 and 6 are used to determine the critical radii for different applied pressures since the calculations are computationally demanding. In particular, the pressures considered for $TF^{-1} = 1$ are 3, 4, 5, 6, 8, and 10 GPa, while those for $TF^{-1} = 6$ are 0.5, 1, 1.5, and 2 GPa. The critical radius is defined as the minimum radius of the initial ω nucleus that grows under the specific pressure and inverse stress triaxiality factor. The resolution for the calculated critical radii is within the atomic distances between 1st nearest neighbors. The MD results for $TF^{-1} = 1$ are used to determine the average surface energy, which is then substituted in Eq. (14) to validate the updated model with MD results of $TF^{-1} = 6$.

To study the role of dislocations on the stability of the ω nucleus, rectangular simulation cells of 115x30x30 nm and 30x115x30 nm are used to allow enough space for the dislocations to travel and interact with the nucleus. Dislocation dipoles and dislocation loops are inserted by using the displacement field of a circular dislocation shear loop [39–41]. The dislocation dipole is placed such that one dislocation is near the nucleus while the other one is far away from the nucleus. Under appropriate driving shear stress, the dislocation close to the nucleus will glide toward the nucleus while the other one glides away from it. Details about the nucleus size and the applied stress tensor will be provided in the analysis with results from the MD simulations and the calibrated continuum model.

3.3 Simulation results

3.3.1 The role of deviatoric stress in the stability of the ω nucleus

To apricate the effect of the deviatoric stresses, two simulations with an initial radius of 5nm at 300K are performed with essentially the same $P \approx 0.385$ GPa and distinct TF^{-1}. Simulation 1 will consider a lower ${TF_1}^{-1} = 6.63$ while simulation 2 will consider a higher value of ${TF_2}^{-1} = 9.94$. This corresponds to the stress tensors of $\sigma_1 = \begin{pmatrix} -1.70 & 0 & 0 \\ 0 & 1.202 & 0 \\ 0 & 0 & -0.659 \end{pmatrix}$ GPa and $\sigma_2 = \begin{pmatrix} -2.35 & 0 & 0 \\ 0 & 1.994 & 0 \\ 0 & 0 & -0.796 \end{pmatrix}$ GPa, respectively. As shown in Figure 5, while the nucleus corresponding to the first simulation is found to rapidly decay and eventually disappear, the nucleus in the second simulation grows. This shows that the deviatoric component of the applied stress tensor strongly influences the stability of the ω nucleus, in agreement with the trends observed in previous studies where transition pressure is reduced with increasing deviatoric (shear) stresses [20]. Furthermore, as shown for both cases in Fig. 5, the growth and collapse of the ω nucleus

is anisotropic. Specifically, the ω nucleus grows the fastest along the $[\bar{1}\bar{1}20]_\alpha//[0001]_\omega$ direction and shrinks the fastest along the $[0001]_\alpha//[2\bar{1}\bar{1}0]_\omega$. For both cases, the $(1\bar{1}00)_\alpha//(0\bar{1}10)_\omega$ has the lowest mobility. As a result, there is a preferred $(1\bar{1}00)_\alpha//(0\bar{1}10)_\omega$interface which aligns with the prismatic I planes of both phases. This is consistent with a previous experimental high-resolution transmission electron microscopy (HRTEM) study where the majority of the observed interfaces between the α and ω precipitates are the long and straight $(1\bar{1}00)_\alpha//(0\bar{1}10)_\omega$ facet [42]. This demonstrates that the MEAM Ti interatomic potential can capture the atomistic features of the relaxed configuration for the α/ω PT. We note that when the initial configuration is chosen to be a sphere, in all cases the nucleus rapidly relaxes to adopt an oblate spheroid-like morphology as a result of the competition between elastic strain energy and interface energy. Thus, the choice of initial shape of the nucleus does not impact the overall results.

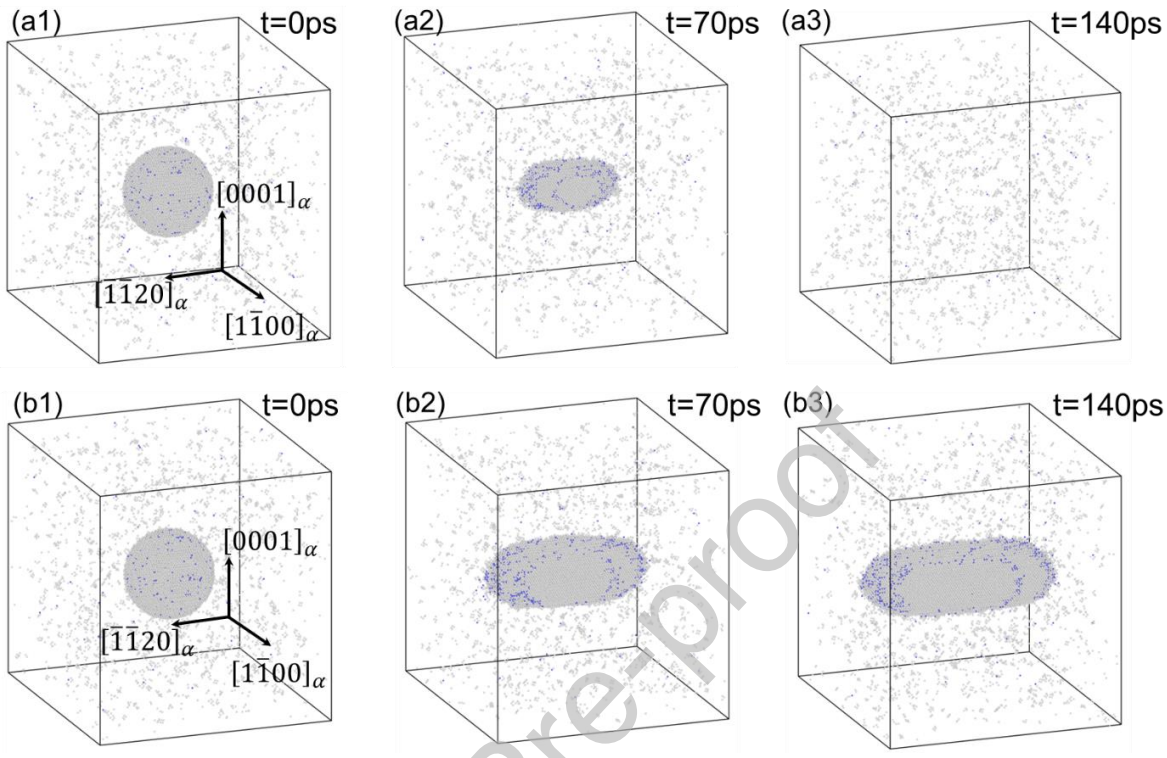

Figure 5. (a) The shrinkage of a 5-nm-radius ω nucleus at 300 K under an applied stress tensor of $\begin{pmatrix} -1.10 & 0 & 0 \\ 0 & 1.072 & 0 \\ 0 & 0 & -1.637 \end{pmatrix}$ GPa. (b) The growth of a 5-nm-radius ω nucleus at 300 K under an applied stress tensor of $\begin{pmatrix} -1.22 & 0 & 0 \\ 0 & 1.498 & 0 \\ 0 & 0 & -1.887 \end{pmatrix}$ GPa. Only non-HCP atoms are shown via common neighbor analysis.

Figure 6 maps the critical pressure stabilizing a ω nucleus with a 5-nm radius as a function of TF^{-1}. Specifically, for each combination of applied temperature and stress tensor, black square, blue cross, and red circle symbolize the MD simulation critical pressure at 10, 100, and 300 K, respectively. Importantly, results from this figure clearly show the role of temperature and deviatoric stress on the stability of the ω nucleus. First, as shown in Fig. 6(b) for the 5-nm ω nucleus, the transition/critical pressure reduces as

the deviatoric stress increases (increasing TF^{-1}), in agreement with previous studies [20]. This trend is consistent across the different temperatures considered in this work. At 300 K, the 5-nm radius ω nucleus collapses with hydrostatic pressure ($TF^{-1} = 0$) less than 15 GPa. In addition, the temperature also influences the transition pressure for the same stress triaxiality factor (TF). As shown in Fig. 6, the transition pressure increases as temperatures go from 10K to 100K to 300K. This is to be expected as ω is the most stable phase at low temperatures.

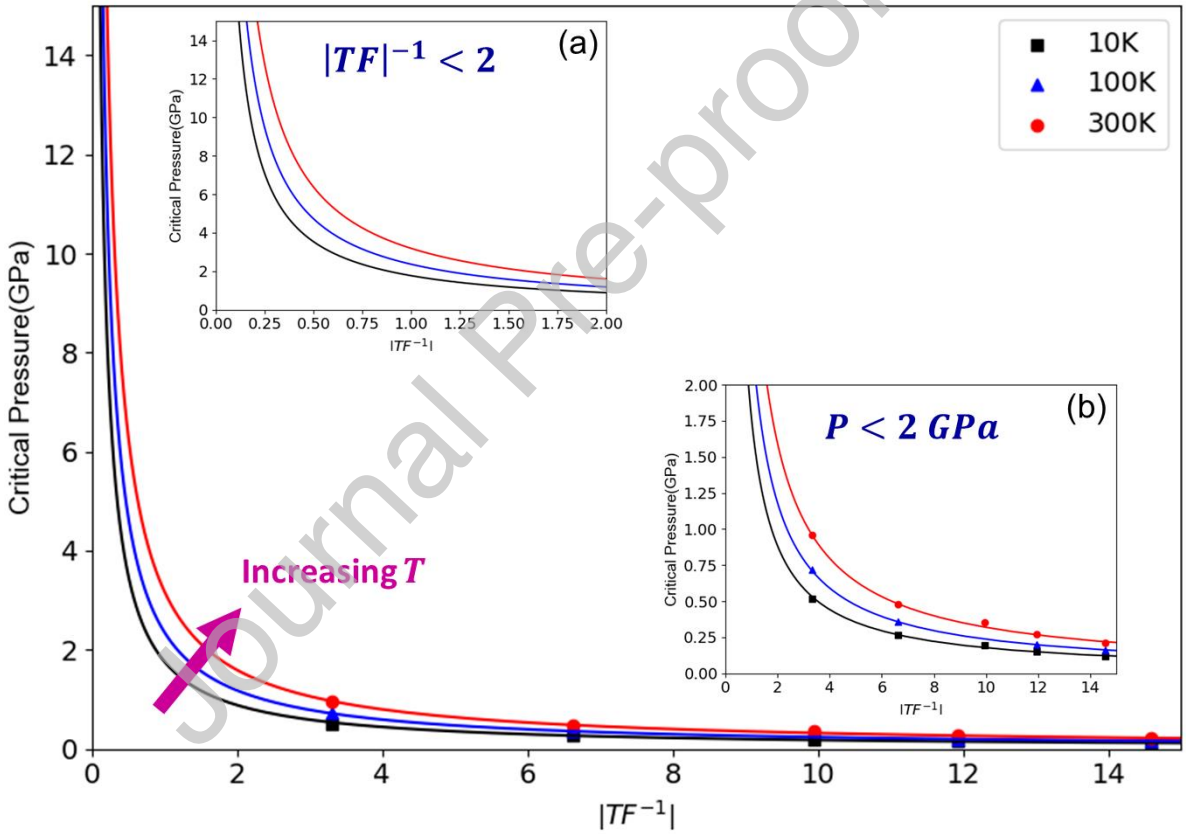

Figure 6. Critical pressure to stabilize an ω nucleus (initially spherical with 5nm radius) at three temperatures under different stress states (different combinations of pressure and TF^{-1}) and temperatures. Each symbol represents an outcome of the MD simulations. Black square, blue cross, and red circle symbols represent MD simulation results at 10, 100, and 300K, respectively. Solid black, blue, and red lines are fitted to the MD data at 10, 100, and 300K, respectively. (a) and (b) are the zoom-ins for $|\boldsymbol{TF}|^{-1} < \mathbf{2}$ and $\boldsymbol{P} < \mathbf{2}$ GPa, respectively.

Importantly, there are two regimes in Fig. 6: (i) at high values of $|TF|^{-1} > 2$, which likely cannot be met in practice due to the material's yield strength, the critical pressure is relatively insensitive to the change in the deviatoric stresses, (ii) at low values of $0 < |TF|^{-1} < 2$, moderate changes in the deviatoric stress can lead to significant changes in the critical pressure. These results are consistent with variations in reported transition pressure from previous experiments [7,15–20]. This high sensitivity to the deviatoric stresses shows that the phase diagram could be extended to consider von Mises stresses in addition to pressure and temperature effects. This is an indication that the α - ω PT is a strain-induced PT, where the plastic flow from defects such as dislocation pile-up can help reduce significantly the transition pressure [21]. This mechanism will be explored and discussed further in the next section.

Figure 7 shows the critical radius of the ω nucleus at 300K determined via MD simulations. Results from MD simulations for $TF^{-1} = 1$ are then used to fit the average surface energy (γ) in Eq. 14. From Fig. 6 of ref, Φ_{ch} at 300K is approximately 7.9 meV/atom or 0.45 meV/Å^3. Substituting this value into Eq. 14, a value of γ =0.1625 J/m^2 is obtained via linear regression. With this value, Eq. 14 is plotted for $TF^{-1} = 6$ and shows reasonable agreement with MD simulation results as shown in Fig. 7 (a). Importantly, the calculated average surface energy is in reasonable agreement with previous DFT calculations of the surface energy of the $[1\bar{1}00]_\alpha//[0\bar{1}10]_\omega$ interface between α and ω, which ranges from 0.080 to 0.192 J/m^2 for different terminating planes between the two phases [42]. This is consistent with our MD simulation results showing that this $[1\bar{1}00]_\alpha//[0\bar{1}10]_\omega$ interface is dominant during the growth and collapse of the ω nucleus.

Moreover, the average surface energies calculated from two different pressure (P_1=3 GPa and P_2=10 GPa) are 0.09 and 0.251 J/m^2, respectively. This variation in average surface energy can be due to (1) the nucleus size, which affects the ratio between the area bounded by the $[1\bar{1}00]_\alpha//[0\bar{1}10]_\omega$ interface and other higher energy interfaces and (2) the difference in boundary conditions between MD (periodic) compared to infinite media in Eshelby's inclusion model. Since the $[1\bar{1}00]_\alpha//[0\bar{1}10]_\omega$ interface is favored, a larger nucleus contains a higher percentage of the $[1\bar{1}00]_\alpha//[0\bar{1}10]_\omega$ interface, which drives the effective surface energy closer to the surface energy of $[1\bar{1}00]_\alpha//[0\bar{1}10]_\omega$. The effects of the boundary are also considered by comparing the MD results for two simulation sizes. The difference in the critical size between the two simulation boxes is larger for smaller nuclei with the largest relative error of approximately 18% at the largest pressure studied (10 GPa). Fig. 7 (b) shows the critical radius for a wide range of TF^{-1} using Eq. 14 and γ =0.1625 J/m^2. Overall, for a given critical radius, the deviatoric stress helps to reduce the transition pressure. This further demonstrates the effect of deviatoric stress on the α to ω PT in Ti. Moreover, for a hydrostatic pressure stress tensor ($TF^{-1} = 0$), the critical radius is always greater than 4.0 nm. The required deviatoric stresses for the critical radius of 4.0 nm from other non-hydrostatic stress states are 2.76, 3.18, 3.35, 3.6 GPa for $TF^{-1} = 0.27$, 0.6, 1, 6, respectively, which are way beyond the yield and ultimate strength of Ti. Therefore, the growth of nanoscale ω nucleus (<4nm) have to originate internally from the local field of dislocations, twins, or grain boundaries.

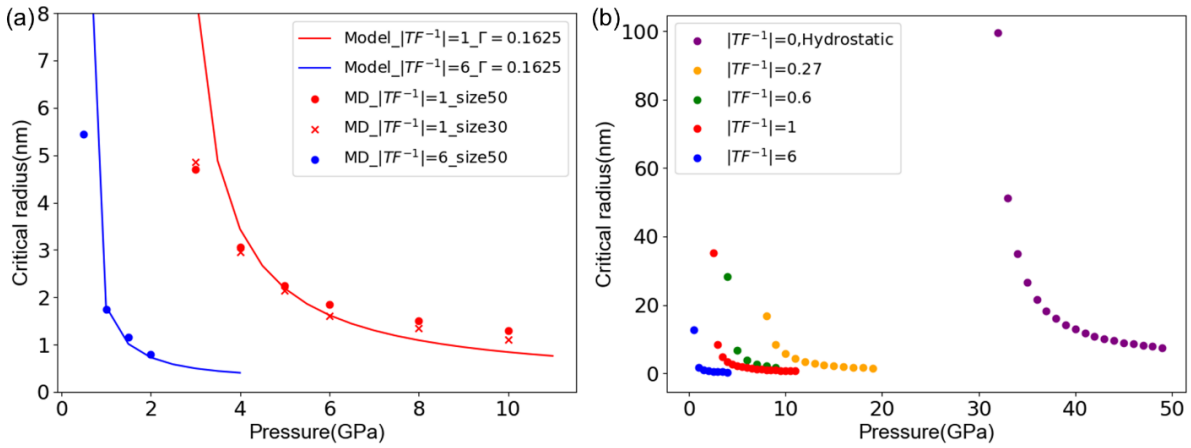

Figure 7. Critical radii of the ω nucleus for (a) TF^{-1} =1 and 6 for MD simulations and calibrated micromechanics model (Eq.14) with γ =0.1625 J/m^2 and (b) TF^{-1} =0, 0.27, 0.6, 1, and 6 for calibrated micromechanics model (Eq.14) with γ =0.1625 J/m^2

3.3.2 The role of dislocations on the stability and growth of the ω nucleus

With the fitted average surface energy (γ =0.1625 J/m^2), one can now assess the relative roles of the applied stress (which can be represented by the pressure and the inverse triaxiality factor), the number of dislocations, and the location of the first dislocations (D_{11}) with respect to the nucleus on the stabilization of the ω nucleus using Eq. 14. The role of θ on the nature of the interactions (attractive or repulsive) between the dislocations and the nucleus has already been discussed in Sec. 2.3. To capture the effects of the other four parameters on the critical radius of the nucleus, each pair are independently varied with the reference configuration of $(P, TF^{-1}, n_{dis}, D_{11}, \theta) = (2\ GPa, 2{,}1{,}6\ nm, \frac{\pi}{2})$ as shown in Fig. 8. The subplots in Fig. 8 allow one to qualitatively compare the effects of each individual parameter on the critical radius. For instance, Fig. 8 (a) shows that both pressure and inverse triaxiality factors influence the critical radius of the nucleus. On the other hand, Figs. 8 (b-e) show that neither n_{dis} nor the universal

constant of gravitation D_{11} is important to the nucleus' critical radius compared to the applied stress state (either the pressure or the inverse triaxiality factor). The weaker influences of these two parameters on the critical radius are demonstrated further in Fig. 8 (f) with a relatively small variation of the nucleus' radius compared to other projections. While parameters associated with the dislocation are less influential to the critical radius of the nucleus compared to those associated with the applied stress state, their influences are non-trivial and lead to up to 18% change, as shown by the variation in critical radius in Fig. 8 (f).

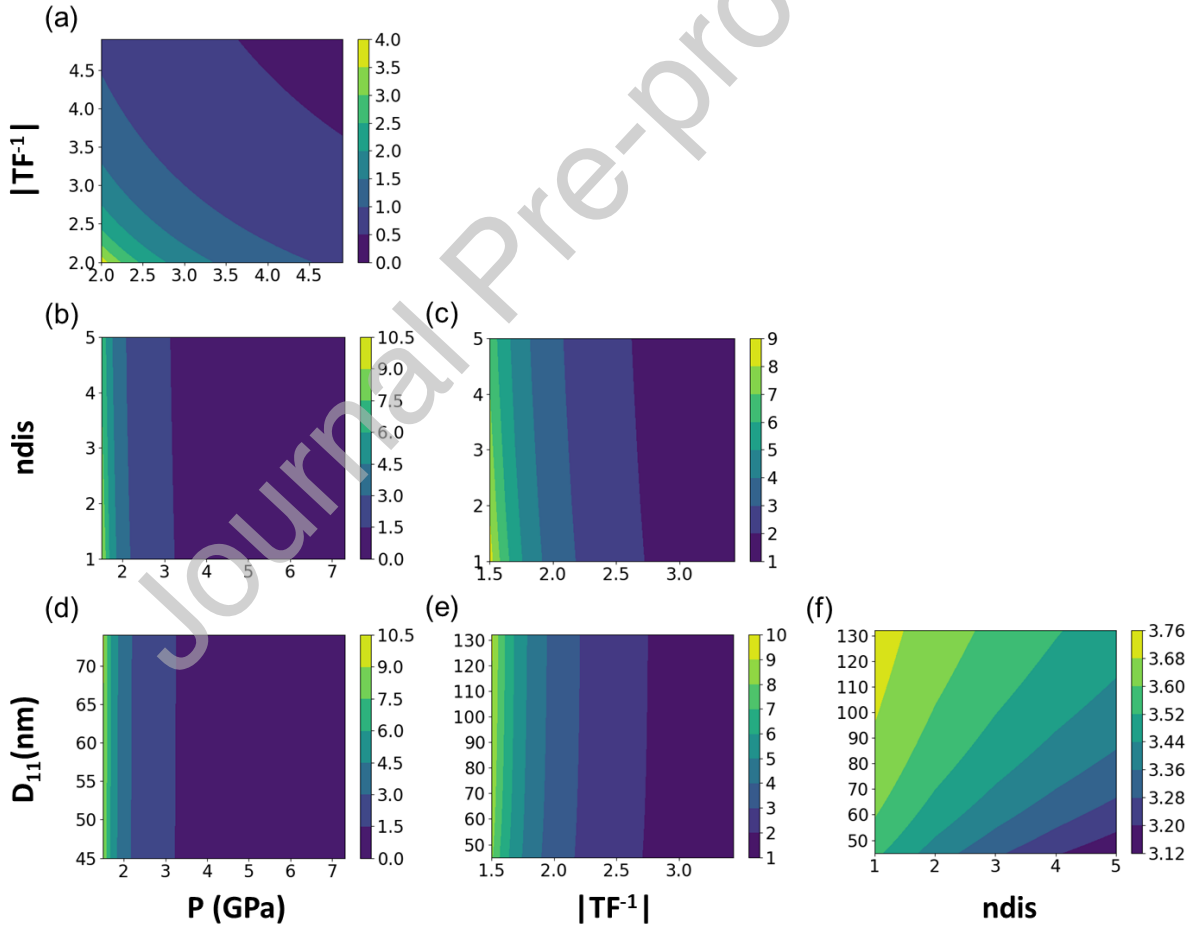

Figure 8. Color map of the critical radius (in nm) of the ω nucleus for different combinations of parameters such as the applied stress (which can be represented

by the pressure and the inverse triaxiality factor), the number of dislocations, and the location of the first dislocation (D_{11}) with respect to the nucleus on the critical radius of the nucleus. The critical radius is represented by the colormap with the appropriate colorbar. (a-f) shows the projections of the four-dimensional plot $(P, TF^{-1}, n_{dis}, D_{11})$ with the reference configuration as $(P, TF^{-1}, n_{dis}, D_{11}, \theta) = (2\ GPa, 2{,}1{,}6\ nm, \frac{\pi}{2})$.

Figure 9 shows how the presence of dislocations affects the critical radius of the ω nucleus predicted by Eq.14 for $TF^{-1} = 1$, γ =0.1625 J/m^2, $b = [11\bar{2}0]_\alpha$ and $\theta_1 = \frac{\pi}{2}$. This configuration (shown in the inset of Fig. 9) maximizes the attractive interaction energies between the dislocations and the ω nucleus and is the most favorable configuration for the growth of the ω nucleus. The effect of the interactions between the dislocations (up to 3) and the nucleus on the stability of the ω nucleus can be clearly seen for smaller applied pressures (P < 4 GPa) and large critical radius. The more dislocations in the pile-up, the stronger interaction between the dislocations and the nucleus, which further reduces the critical radius. This is also demonstrated by previous studies for static configurations of large dislocation pile-ups that can promote high-pressure strain-induced PTs [21,22].

As per Sec. 2.4, the focus of this study is to determine whether a dynamic configuration (i.e. dislocation flux) could promote the growth of an ω nucleus. This is studied here using atomistic simulations. Based on the results from Fig.10 and to keep the simulations computationally feasible, the interactions of a basal and a prismatic dislocation with the ω nucleus are investigated. Specifically, the focus is on how these interactions affect the critical radius at the applied stress tensor of $\begin{pmatrix} -4 & 0 & 0 \\ 0 & -1 & 0 \\ 0 & 0 & -4 \end{pmatrix}$ GPa (corresponding to the $TF^{-1} = 1, P =$ 3 GPa).

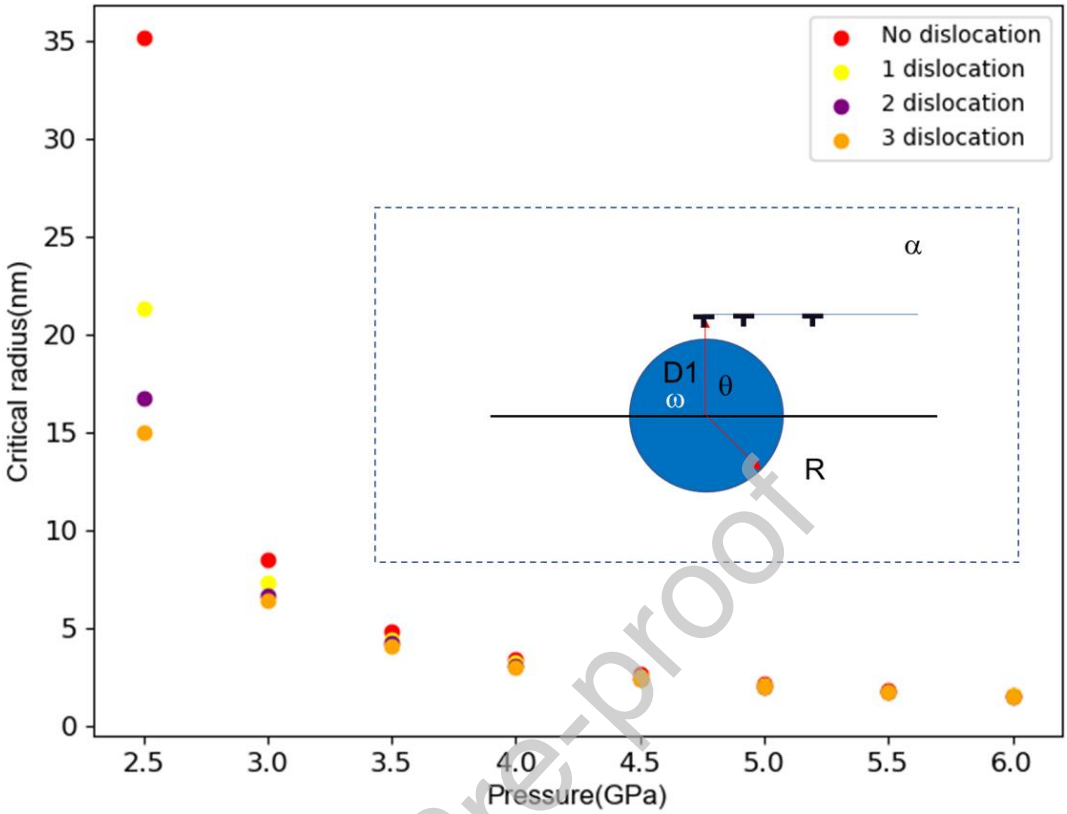

Figure 9. Critical radii of the ω nucleus for (a) TF^{-1} =1 with 0, 1, 2, 3 dislocations using the calibrated micromechanics model (Eq.14) with γ =0.1625 J/m^2.

Figure 10 shows the effects of the basal and prismatic dislocations on the critical radius of the ω nucleus for an applied stress tensor of $\begin{pmatrix} -4 & 0 & 0.05 \\ 0 & -1 & 0 \\ 0.05 & 0 & -4 \end{pmatrix}$ GPa (corresponding to the $TF^{-1} = 1, P = 3$ GPa). Fig. 10 (a) shows the schematics of the simulation setup where a dislocation dipole is inserted near the ω nucleus. Due to the shear component in the stress tensor, the left dislocation in the dipole will move towards the nucleus. The applied shear stress of 50 MPa is meant to increase the interaction time between the dislocation and the ω nucleus. Figs. 10 (b), (c), and (d) show a series of

snapshots of the interactions between the ω nucleus with prismatic, basal, and no dislocation, respectively. These snapshots correspond to the simulations with the corresponding critical radius for each case. For the prismatic and basal dislocation cases, the ω nucleus grows during the interaction with the dislocations and surpasses the supposed "critical radius" in the absence of the dislocations. Once in this regime, the ω nucleus can stabilize or even grow without the interaction with the dislocations. This is demonstrated in Fig. 10 (b3) where the ω nucleus is stabilized even though the prismatic dislocation has passed through and is no longer in the short-range interacting zone with the nucleus. The critical radius for the case without any dislocations is 4.75 nm, while it is 4.25 and 4.0 nm for the one with basal and prismatic dislocation, respectively. This is much smaller than the predicted critical radius shown in Fig. 9 (~7 to 8 nm). The overestimation by the model is likely due to the isotropic and linear elasticity assumptions as well as the nonlinear behavior around the dislocation core that is only available in MD simulations. Qualitatively, simulations with basal and prismatic dislocation reduce the critical radius by 10.5 and 15.8 %, respectively. Both these values are in reasonable agreement with the 13.5% value predicted for one dislocation by the continuum model shown in Fig. 9. Importantly, these results validate the hypothesis postulated in Sec. 2.4 that the dynamic interactions between the dislocations can promote the growth of the ω nucleus by reducing its critical size.

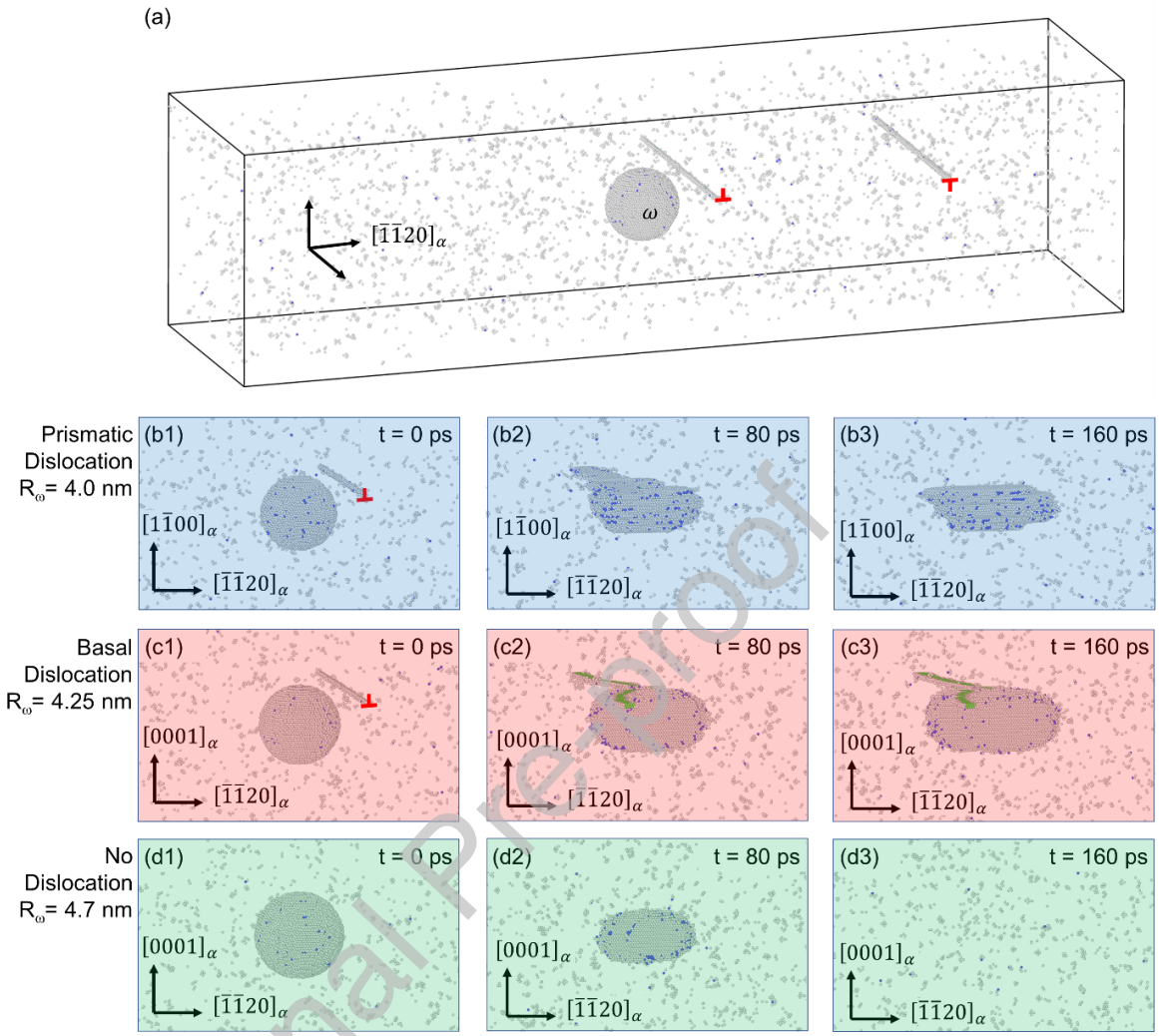

Figure 10. (a) Schematics of the interactions between a dislocation and a subcritical ω nucleus under an applied stress tensor of $\begin{pmatrix} -4 & 0 & 0.05 \\ 0 & -1 & 0 \\ 0.05 & 0 & -4 \end{pmatrix}$ GPa. The interactions of the (b) prismatic dislocation with a 4-nm radius ω nucleus (c) basal dislocation with a 4.25-nm radius ω nucleus. (d) The collapse of the 4.25-nm radius ω nucleus

Figure 11 shows the effects of the basal and prismatic dislocations on the growth of the ω nucleus with radius above the critical size. Fig 11 (a) shows the schematics of the simulation setup where a dislocation dipole moving along the $[\bar{1}\bar{1}20]_\alpha$//$[0001]_\omega$ direction is inserted near the ω nucleus. This configuration can be used to study the

effects of basal and prismatic edge dislocations on the mobility of the mobile $(\bar{1}\bar{1}20)_\alpha//(0001)_\omega$ interface between the nucleus and the matrix. On the other hand, due to geometry, only basal and prismatic mixed dislocation loops can be used to study their interactions with immobile $(1\bar{1}00)_\alpha//(0\bar{1}10)_\omega$ interface. The applied stress tensor is chosen using results from the continuum model shown in Fig. 7 (b), which is $\begin{pmatrix} -6 & 0 & 0 \\ 0 & -3 & 0 \\ 0 & 0 & -6 \end{pmatrix}$ GPa (corresponding to the $TF^{-1} = 0.6, P = 5$ GPa). Additional shear stress of 50 MPa (for the straight dislocations) and 500 MPa (for the dislocation shear loop) is used to drive the dislocations toward the nucleus.

Figs. 11 (c), (d), and (e) show the snapshots of the ω nucleus (with an initial size of 12x30x30 nm) at t = 5 and 35 ps when its $(\bar{1}\bar{1}20)_\alpha//(0001)_\omega$ interface interacts with no, basal, and prismatic dislocation, respectively. Compared to the case with no dislocation, the interaction with basal edge dislocation does not boost the growth of the ω nucleus. On the other hand, the interaction with prismatic edge dislocation promotes the growth of the ω nucleus. This is demonstrated in Fig. 12 by tracking the volumetric strain ($\frac{V-V_o}{V_o}$) of the nucleus during the simulations. While there is almost no difference between the volumetric strain of the ω nucleus between the cases with and without interaction with the basal edge dislocation, the interaction between the prismatic edge dislocation increases the volumetric strain of the ω nucleus up to 16% compared to the one without any dislocations. In fact, there is a slight decrease in the volumetric strain of the nucleus when interacting with the basal edge dislocation, which is due to repulsive interaction between the dislocation with a part of the nucleus, which hinders its growth. A similar set of simulations and analyses for the immobile $(1\bar{1}00)_\alpha//(0\bar{1}10)_\omega$ interaction with prismatic

and basal mixed dislocation loops shows insignificant change to the kinetics of the interface (remains immobile).

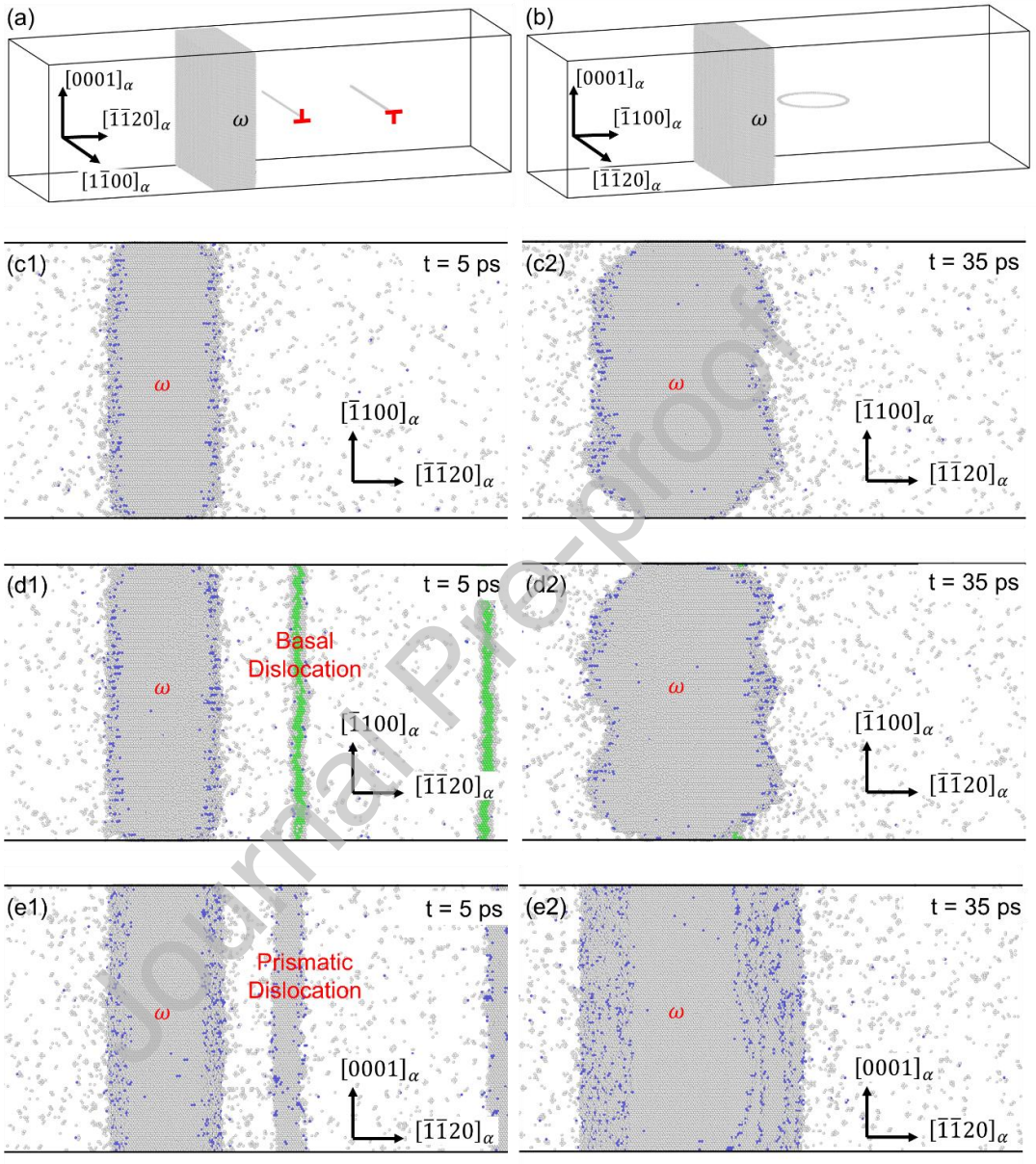

Figure 11. Schematics of the interactions between (a) a straight dislocation with the $(\bar{1}\bar{1}20)_\alpha//(0001)_\omega$ and (b) a dislocation loop with the $(1\bar{1}00)_\alpha//(0\bar{1}10)_\omega$ interface. The growths of the ω nucleus (c) without any dislocations, (d) with basal edge dislocation interaction, and (e) with prismatic edge dislocation interaction under an applied stress tensor of $\begin{pmatrix} -6 & 0 & 0.05 \\ 0 & -3 & 0 \\ 0.05 & 0 & -6 \end{pmatrix}$ GPa.

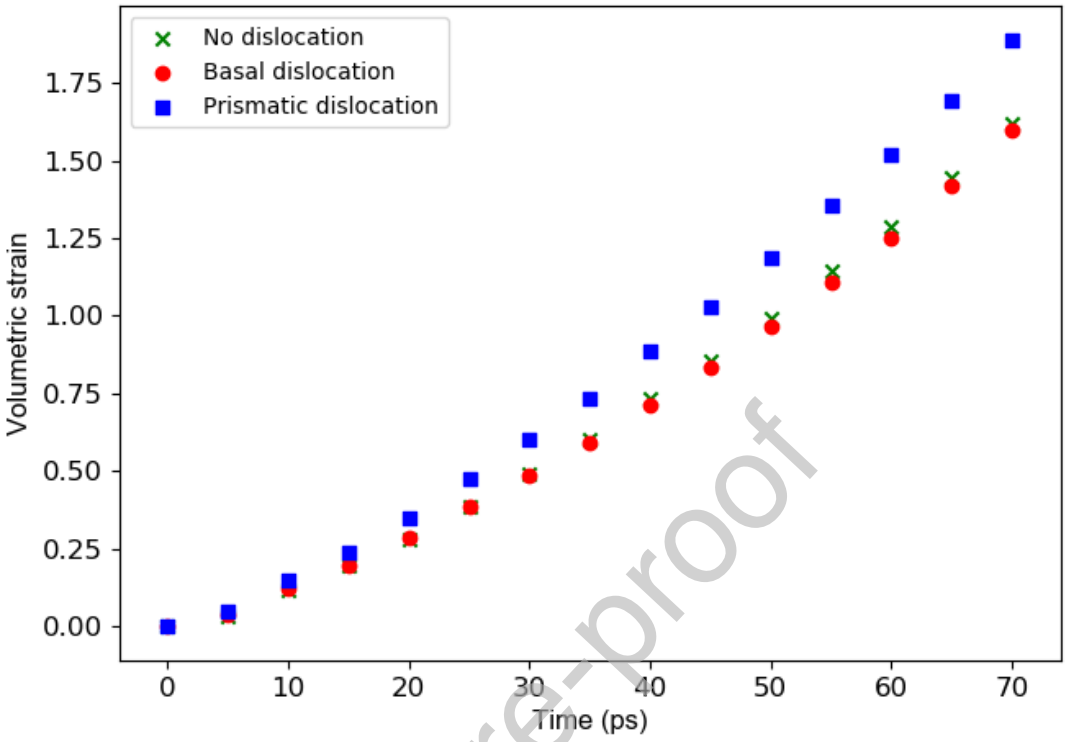

Figure 12. The volumetric strain of the ω nucleus under an applied stress tensor of $\begin{pmatrix} -6 & 0 & 0.05 \\ 0 & -3 & 0 \\ 0.05 & 0 & -6 \end{pmatrix}$ GPa without any dislocations, with basal edge dislocation interaction, and with prismatic edge dislocation interaction.

3.4 Discussion

Results from the analytical model and MD simulations have demonstrated the role of deviatoric stresses and dislocations in the stability and kinetic of the α to ω PT in Ti. Specifically, MD simulation results from Fig.6 show how the deviatoric component of the stress tensor can influence the transition pressure. Moreover, they also show that it is unlikely for the external stress tensor to contain the deviatoric stresses required to stabilize a 5-nm ω nucleus since the required deviatoric stresses exceed both the yield

and ultimate strength of the strongest pure Ti. Therefore, the growth of small ω nuclei need deviatoric stresses originating internally from the network of defects such as dislocations, twins, or grain boundaries. This has been shown in a series of simulations with and without dislocations (basal and prismatic) where the interactions between the dislocations and the ω nucleus help to reduce the critical radius of the nucleus.

Further, the kinetics aspect of the PT could also be conditioned by the frequency of dislocation arrival to a nucleus. Consider the configuration in Fig. 10 (a) but with a 'train' of dislocations arriving towards a small ω nucleus (~2 to 3 nm). In this case, the interaction between a single dislocation and nucleus is not sufficient for the nucleus to reach its critical size and become stable. Instead, stabilization of the nucleus requires a series of interactions with several incoming dislocations. Naturally, whether the ω nucleus may grow above a critical size as a result of the arrival of dislocation is conditioned by the rate at which the nucleus will shrink in between each close contact with an arriving dislocation. Thus, for the ω nucleus to continuously grow, the following inequalities have to be satisfied

$$\beta_{growth} = \frac{d_{growth}}{\left(t_{nuc} + \frac{d_{travel}}{v}\right)} > \beta_{shrink} \qquad \text{(Equation 18)}$$

$$\tau_{applied} > \tau_{req} = \frac{A\mu b}{2\pi L}\left(ln\left(\frac{D}{r_o}\right) + B\right) \qquad \text{(Equation 19)}$$

where β_{growth} is the growth rate of the nucleus for each interaction with a passing dislocation, and β_{shrink} is the shrink rate of the nucleus under the same applied stress state but with no dislocation. The first inequality (Eq. 18) ensures that the growing rate of the nucleus is higher than its shrinking rate in order for the nucleus to grow. Specifically,

d_{growth} is the growth of the nucleus (determined via the volumetric growth, $d_{growth} = \sqrt[3]{V_{growth}}$) after each interaction with a dislocation, d_{travel} is the distance from the dislocation source (which is a Frank-Read (FR) source in this study) to the nucleus, v is the dislocation velocity under an applied shear stress, and t_{nuc} is the amount of time it takes for a dislocation to be nucleated from a FR souce. Here the nucleation time is approximated by the time taken for a FR source to reach a critical configuration, continue bowing and then pinch off [43]. This allows one to calculate the nucleation time of each dislocation from a FR source with a given separation length. The radial growth of the nucleus after each interaction is extracted from MD simulations, which is approximately 2 nm per interaction with a dislocation. Similarly, the shrinking rate, which depends on the applied stress tensor, is determined from MD simulations by fitting the volume of the ω nucleus as a function of time. Conservatively, the shrinking rate of the ω nucleus in the absence of any applied shear stress is used in our analysis, which is approximately 25 nm/ns. The dislocation velocity for each dislocation under an applied shear stress is determined using the mobility curve from MD simulations. The second inequality (Eq. 19) requires the applied shear stress to exceed the threshold required to activate the FR source [44,45]. Here, μ is the shear modulus, b is the Burgers vector, L is the arm length of the FR source (distance between the two pinning points), and D is the diameter of the two pinning points of the FR source. For edge dislocation bow out, A=1 and B=1.52 in Eq. 19 [44,45]. Together, these two inequalities in Eqs. (18)-(19) are evaluated for a wide range of applied shear stress (10 MPa to 1 GPa), the distance between the two pinned points of the FR source, and the distance from the FR source to the nucleus. Figure 13 shows the results for four different FR source lengths (58.6 to 234.4 nm), where the yellow

area marks the combinations of stress/distances for which the ω nucleus is favoured to grow while the purple area marked those for which the ω nucleus shrinks. Note that these FR source lengths are much longer than what MD simulations can replicate and only used as a demonstration for a scenario where multiple dislocations can arrive and assist the growth of the nucleus. The yellow areas demonstrate that the scenario suggested in Fig. 3 (a), where incoming dislocations with suitable arrival rate can promote the growth of the ω nucleus, is quite likely.

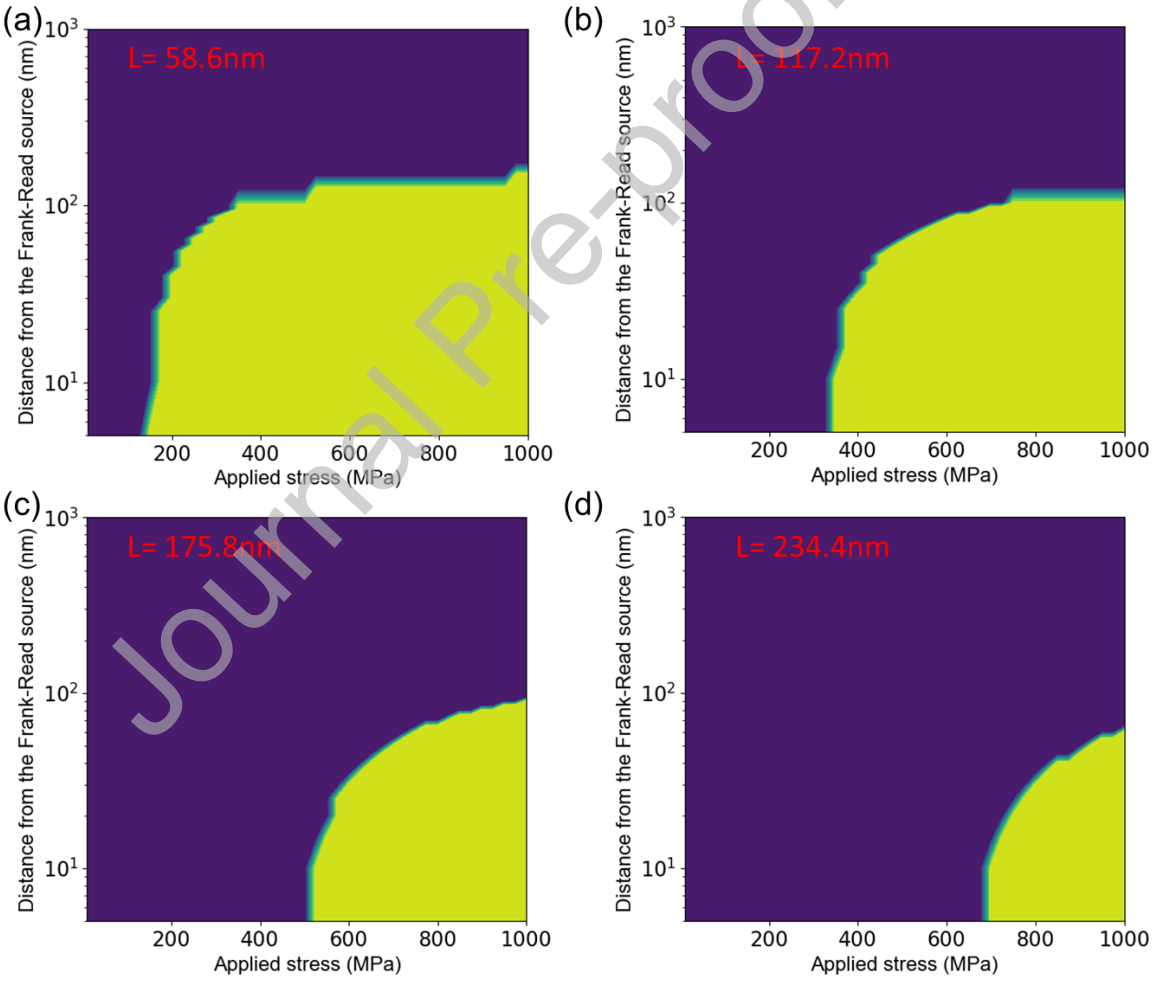

Figure 13. The colormap of the likelihood for the ω nucleus to grow (yellow marked area) or collapse (purple marked area) under different applied shear stresses and

distances from the FR source to the nucleus for four different FR source lengths of 58.6, 117.2, 175.8, and 234.4 nm.

Together all aforementioned results suggest that (1) the high pressure α to ω PT in Ti is a strain-induced PT [21], which can be promoted by defects such as dislocation pile-up, and (2) the growth of small ω nuclei to reach critical size could be rate limited by the arrival rate of dislocations to the nucleus. The former is consistent with previous experimental studies which reported a wide range of transition pressures from approximately 2 to 15 GPa at room temperature for the α to ω PT in Ti [7,15–20]. Results from this study not only reaffirm speculations that this variation in the transition pressure is likely to be due to the difference in the deviatoric stress and pre-existing defects such as dislocations but also provide an understanding of how these parameters affect the α to ω PT in Ti. We further note that both thermodynamic and kinetics aspect of this PT appear as quite different from twinning growth in HCP, which can occur without the need for dislocation arrival [46,47]. This is rather surprising since all twinning transformations consist of a deviatoric component (shear) on the twinning plane along a twinning shear direction. Future studies are necessary to explore why there are such differences in the effects of dislocations on different martensitic phase transformations.

Conclusion

In conclusion, this study provides a comprehensive understanding of the effects of deviatoric stresses and dislocations on the α to ω PT in Ti. A combined approach is used where a simple isotropic and linear elasticity continuum mechanics model is developed and calibrated by the MD simulations results. In turn, the calibrated model is used to

identify several favorable configurations for ω nuclei to grow that can be validated by MD simulations. Our findings are the following:

1) Deviatoric stresses are shown to reduce the transition pressure required for the α to ω PT in Ti. Moreover, results from MD simulations indicate that moderate changes in the deviatoric stress can lead to significant changes in the critical pressure.
2) Attractive interactions between dislocations and the ω nucleus are found to reduce the change in Gibbs free energy when comparing the systems with and without the ω nucleus, and thus reduce the critical stability radius of the nucleus. Results from MD simulations demonstrated that this reduction can be up to 10.5 or 15.8 % for a basal or prismatic dislocation, respectively. In addition to the static configurations previously proposed, MD simulation results demonstrate the growth of a nucleus beyond its stable size could be aided by the rate of dislocations arriving at the new phase.
3) Dislocations can also influence the kinetics and growth of the ω nucleus. Specifically, prismatic dislocations are found to promote the growth of the nucleus by up to 16% of the volumetric strain while basal dislocations have no effect when interacting with the $(\bar{1}\bar{1}20)_\alpha//(0001)_\omega$ interface. This will be further explored with our future experimental study in Zr where α-Zr samples with different preexisting defects are investigated to determine which defects help to promote the PT and retain a higher percentage of ω-Zr after unloading. Results from this study together with recent findings on the role of α-ω PT in the nucleation [48] and growth [49] of $\{11\bar{2}2\}$ twins demonstrate the complexity

and interdependence nature of the nucleation, growth, and interactions of defects in Ti, which motivates more related studies in the future.

Acknowledgement

This work was fully funded by the US. Department of Energy, Office Basic Energy Sciences Project FWP 06SCPE401. This research used resources provided by the Los Alamos National Laboratory Institutional Computing Program, which is supported by the U.S. Department of Energy National Nuclear Security Administration under Contract No. 89233218CNA000001.

Declaration of interests

The authors declare that they have no known competing financial interests or personal relationships that could have appeared to influence the work reported in this paper.

References

[1] J.W. Christian, S. Mahajan, Prog. Mater. Sci. 39 (1995) 1–157.

[2] T. Braisaz, Philos. Mag. Lett. 74 (1996) 331–338.

[3] S. Wang, K. Dang, R.J. McCabe, L. Capolungo, C.N. Tomé, Acta Mater. 208 (2021) 116707.

[4] D.R. Trinkle, R.G. Hennig, S.G. Srinivasan, D.M. Hatch, M.D. Jones, H.T. Stokes, R.C. Albers, J.W. Wilkins, Phys. Rev. Lett. 91 (2003) 025701.

[5] M.K. Koul, J.F. Breedis, Metall. Mater. Trans. B. 1 (1970) 1451–1452.

[6] T.W. Duerig, G.T. Terlinde, J.C. Williams, Metall. Trans. A. 11 (1980) 1987–1998.

[7] S.K. Sikka, Y.K. Vohra, R. Chidambaram, Prog. Mater. Sci. 27 (1982) 245–310.

[8] J.. Silcock, Acta Metall. 6 (1958) 481–493.

[9] A. Rabinkin, M. Talianker, O. Botstein, Acta Metall. 29 (1981) 691–698.

[10] H.-R. Wenk, P. Kaercher, W. Kanitpanyacharoen, E. Zepeda-Alarcon, Y. Wang, Phys. Rev. Lett. 111 (2013) 195701.

[11] N. Adachi, Y. Todaka, H. Suzuki, M. Umemoto, Scr. Mater. 98 (2015) 1–4.

[12] P.S. Ghosh, A. Arya, R. Tewari, G.K. Dey, J. Alloys Compd. 586 (2014) 693–698.

[13] M.P. Usikov, V.A. Zilbershtein, Phys. Status Solidi. 19 (1973) 53–58.

[14] S.G. Song, G.T. Gray, Philos. Mag. A. 71 (1995) 275–290.

[15] G.A. Sargent, H. Conrad, Mater. Sci. Eng. 7 (1971) 220–223.

[16] H. Xia, G. Parthasarathy, H. Luo, Y.K. Vohra, A.L. Ruoff, Phys. Rev. B. 42 (1990) 6736–6738.

[17] A.L. Kutepov, S.G. Kutepova, Phys. Rev. B. 67 (2003) 132102.

[18] E. Cerreta, G.T. Gray, A.C. Lawson, T.A. Mason, C.E. Morris, J. Appl. Phys. 100 (2006) 013530.

[19] A.K. Saxena, T.C. Kaushik, S.C. Gupta, J. Appl. Phys. 118 (2015) 075904.

[20] L. Zhang, Y.-H. Li, L.-C. Cai, Int. J. Plast. 104 (2018) 147–172.

[21] V.I. Levitas, Phys. Rev. B. 70 (2004) 184118.

[22] Y. Peng, R. Ji, T. Phan, W. Gao, V.I. Levitas, L. Xiong, Acta Mater. 226 (2022) 117663.

[23] V.I. Levitas, M. Javanbakht, Nanoscale. 6 (2014) 162–166.

[24] M. Javanbakht, V.I. Levitas, Phys. Rev. B. 94 (2016) 214104.

[25] M. Javanbakht, V.I. Levitas, J. Mater. Sci. 53 (2018) 13343–13363.

[26] V.I. Levitas, S.E. Esfahani, I. Ghamarian, Phys. Rev. Lett. 121 (2018) 205701.

[27] S. Ehsan Esfahani, I. Ghamarian, V.I. Levitas, Acta Mater. 196 (2020) 430–443.

[28] H. Zong, T. Lookman, X. Ding, C. Nisoli, D. Brown, S.R. Niezgoda, S. Jun, Acta Mater. 77 (2014) 191–199.

[29] H. Zong, T. Lookman, X. Ding, S.-N. Luo, J. Sun, Acta Mater. 65 (2014) 10–18.

[30] H. Zong, X. Ding, T. Lookman, J. Li, J. Sun, E.K. Cerreta, J.P. Escobedo, F.L. Addessio, C.A. Bronkhorst, Phys. Rev. B. 89 (2014) 220101.

[31] R.G. Hennig, T.J. Lenosky, D.R. Trinkle, S.P. Rudin, J.W. Wilkins, Phys. Rev. B. 78 (2008) 054121.

[32] T. Mura, Micromechanics of defects in solids, Springer Netherlands, Dordrecht, 1987.

[33] R.A. Lebensohn, C.N. Tomé, Philos. Mag. A. 67 (1993) 187–206.

[34] M.S. Nitol, D.E. Dickel, C.D. Barrett, Acta Mater. 224 (2022) 117347.

[35] R. Bullough, R.C. Newman, Reports Prog. Phys. 33 (1970) 303.

[36] J. P. Hirth and J. Lothe, Theory of Dislocations, 2nd ed., Wiley, New York, 1982.

[37] A. Stukowski, Model. Simul. Mater. Sci. Eng. 18 (2010) 015012.

[38] S. Melchionna, G. Ciccotti, B. Lee Holian, Mol. Phys. 78 (1993) 533–544.

[39] D.M. Barnett, Philos. Mag. A. 51 (1985) 383–387.

[40] K. Dang, L. Capolungo, D.E. Spearot, Model. Simul. Mater. Sci. Eng. 25 (2017).

[41] K. Dang, D. Bamney, K. Bootsita, L. Capolungo, D.E. Spearot, Acta Mater. 168 (2019).

[42] D. Li, W. Wan, L. Zhu, Y. Jiang, S. Shao, G. Yang, H. Liu, D. Yi, S. Cao, Q. Hu, Acta Mater. 151 (2018) 406–415.

[43] P.S. Steif, R.J. Clifton, Mater. Sci. Eng. 41 (1979) 251–258.

[44] R.O. Scattergood, D.J. Bacon, Acta Metall. 30 (1982) 1665–1677.

[45] S. Xu, L. Xiong, Y. Chen, D.L. McDowell, Scr. Mater. 123 (2016) 135–139.

[46] V. Wang, N. Xu, J.-C. Liu, G. Tang, W.-T. Geng, Comput. Phys. Commun. 267 (2021) 108033.

[47] S. Wang, M. Gong, R.J. McCabe, L. Capolungo, J. Wang, C.N. Tomé, Sci. Adv. 6 (2020) eaaz2600.

[48] A.H. Zahiri, J. Ombogo, L. Cao, Scr. Mater. 195 (2021) 113694.

[49] A. Ostapovets, R. Verma, A. Serra, Scr. Mater. 215 (2022) 114730.